Suppressed Carrier Scattering in CdS-Encapsulated PbS Nanocrystal Films

Pavel Moroz,[†,§] Natalia Kholmicheva,[†,§] Bryan Mellott,[‡] Geethika Liyanage,[§] Upendra Rijal,[§] Ebin Bastola,[§] Kyla Huband,[§] Elena Khon,[†,§] Keith McBride,[§] and Mikhail Zamkov[†,§,*]

[†]The Center for Photochemical Sciences, [‡]Department of Chemistry, and [§]Department of Physics, Bowling Green State University, Bowling Green, Ohio 43403, United States

ABSTRACT One of the key challenges facing the realization of functional nanocrystal devices concerns the development of techniques for depositing colloidal nanocrystals into electrically coupled nanoparticle solids. This work compares several alternative strategies for the assembly of such films using an all-optical approach to the characterization of electron transport phenomena. By measuring excited carrier lifetimes in either ligand-linked or matrix-encapsulated PbS nanocrystal films containing a tunable fraction of insulating ZnS domains, we uniquely distinguish the dynamics of charge scattering on defects from other processes of exciton dissociation. The measured times are subsequently used to estimate the diffusion length and the carrier mobility for each film type within the hopping transport regime. It is demonstrated that nanocrystal films encapsulated into semiconductor matrices exhibit a lower probability of charge scattering than that of nanocrystal solids cross-linked with either 3-mercaptopropionic acid or 1,2-ethanedithiol molecular linkers. The suppression of carrier scattering in matrix-encapsulated nanocrystal films is attributed to a relatively low density of surface defects at nanocrystal/matrix interfaces.

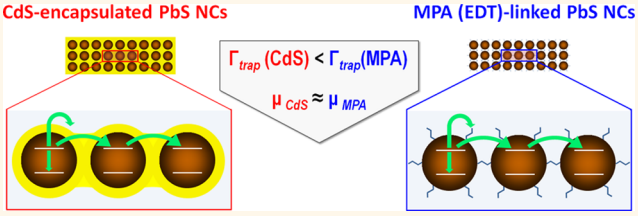

KEYWORDS: photovoltaics · catalysis · nanocrystals · quantum dots

Colloidal semiconductor nanocrystals are emerging as promising nanomaterials for solution-processing of thin-film devices. Due to quantum confinement of electrical charges in these nanostructures, their optoelectronic properties can be continuously tuned *via* the nanoparticle size.[1] This enables the optimization of the film's key characteristics, either by adjusting the band gap of the semiconductor nanocrystal,[2] by enhancing the nanoparticle fluorescence quantum yield through shell growth,[3] or by balancing the driving force at heteromaterial interfaces.[4] Furthermore, processing of thin-film devices from solutions of colloidal nanoparticles is less expensive than traditional methods of film deposition, which rely on high vacuum and high-temperature treatments. Owing to these benefits, a great deal of experimental work in the past decade has been focused on the development of strategies for assembly of colloidal nanocrystals into films and superlattices, as well as on improving nanocrystal films' properties toward practical applications, including lasers,[5−7] solar cells,[8−27] light-emitting diodes (LEDs),[28−36] thermoelectric elements,[37,38] and field-effect transistors.[39−45]

At present, the key issue limiting the performance of nanocrystal devices is related to the poor conductivity of nanocrystal films caused by the energy disorder[46] and charge scattering on imperfectly passivated surface atoms.[47,48] It was previously shown that cationic dangling bonds create trap states below the conduction band minimum, while unpassivated anionic sites result in the formation of traps above the valence band maximum.[49] Because of the high surface-to-volume ratio in semiconductor nanocrystals, the density of such trap states can be significant. As a result, the charge transport in nanoparticle films is hampered by the premature recombination of electrical charges on surface states, which is detrimental to device operation.[27]

Traditionally, nanocrystal solids are fabricated by bridging neighboring nanoparticles with organic or inorganic ligands that render NC films electrically conductive. A potential drawback of this strategy concerns the fact that even a slight imbalance between the number of ligand molecules

* Address correspondence to zamkovm@bgsu.edu.

Received for review April 30, 2013 and accepted July 26, 2013.

Published online July 27, 2013
10.1021/nn402844m

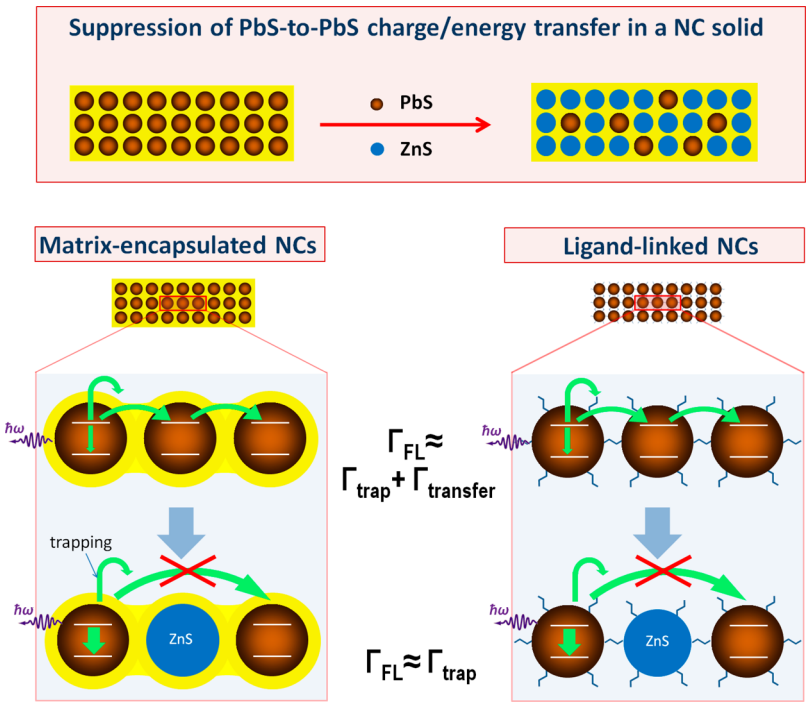

Figure 1. Illustration of the strategy for determining carrier trapping rates in nanocrystal films. The decay of the photoinduced charges in PbS NC films (either ligand-linked or matrix-encapsulated) occurs through several pathways, including radiative recombination, interparticle charge/energy transfer, variable range hopping, and charge trapping on surface dangling bonds. The rates of other processes of exciton dissociation were found to be negligibly slow. When wide band gap ZnS NCs are introduced into the PbS NC film, the interparticle charge and energy transfer become strongly suppressed, such that the resulting fluorescence lifetime becomes dominated by trapping of photoinduced charges on surfaces (see text). Consequently, the measured fluorescence lifetime in PbS NC films saturated with ZnS nanoparticles approaches that of carrier surface trapping time.

and surface atoms results in a considerable population of states within the nanocrystal band gap, causing scattering of electrical charges. As was demonstrated by a recent study from the Sargent group, the density of trap states just below the conduction band edge for either organically or inorganically cross-linked nanocrystal films is on the order of 10^{17} cm^{-3} eV^{-1}.[50] This figure is at least 3 orders of magnitude greater than the trap state density of most single-crystalline semiconductors. While a hybrid passivation strategy[27] involving a combination of organic and small inorganic ligands was recently shown to reduce the density of traps in nanocrystal films down to 2×10^{16} cm^{-3} eV^{-1}, a more radical treatment of surface states is still necessary for the development of competitive thin-film NC devices, which electrical conductivity is on the par with rival technologies operating in the band transport regime.

A promising alternative to a traditional, ligand-based assembly of nanoparticle solids is provided by ligand-free film deposition routes,[51−55] which rely on the use of a stable inorganic medium for passivating nanocrystal surfaces in a solid. Of particular interest is a recently reported matrix encapsulation strategy, which employs a wide band gap CdS or ZnS semiconductor matrix to encapsulate arrays of evenly spaced CdSe or PbS nanocrystals.[53,54] The matrix medium efficiently preserves the quantum confinement of embedded nanocrystals while protecting their surfaces from interactions with external environment. The key advantage of such an encapsulation scheme is the passivation strategy itself, which forces every cation and anion on the surface of semiconductor nanocrystals to be heteroepitaxially bonded to their respective counterions of the CdS matrix. As a result, trap states cannot form directly on the surface of nanocrystals. While charge trapping can still occur on the boundaries of the matrix itself, the probability of this process is relatively low since charges are confined by the potential barrier of the matrix. Consequently, one can expect that the formation of trap states in matrix-encapsulated nanocrystal films will be suppressed relative to ligand-linked NC solids.

Here, we compare electrical transport characteristics of matrix-encapsulated and ligand-linked nanocrystal solids by measuring the corresponding rates of charge trapping and exciton dissociation processes. To distinguish the dynamics of defect trapping from other mechanisms of exciton decay, we introduce a controlled amount of "insulating" ZnS nanoparticles into a film of PbS NCs, which serves to suppress the transfer of excitation energy between PbS dots (see Figure 1). In this geometry, the photoinduced charges in PbS domains of ZnS/PbS NC films are forced to dissipate

primarily through trapping on surface states, whose dynamics can then be monitored *via* fluorescence (FL) intensity decay.

By varying the fraction of ZnS nanoparticles in PbS NC films, we demonstrate that the rate of carrier trapping on surface defects is slower for matrix-encapsulated solids than in the case of films where nanocrystals are connected by ligands. In addition to charge scattering rates, the observed dynamics of carrier decay was used to determine the rates of exciton dissociation processes, which were then converted into carrier mobilities and diffusion lengths for different film architectures. It was found that CdS-encapsulated PbS NC films yielded the highest carrier diffusion length, followed by 3-mercaptopropionic acid (MPA)-linked PbS films featuring Cl surface passivation. Meanwhile, 1,2-ethanedithiol (EDT)-linked PbS NC films gave rise to the shortest length of carrier diffusion. Overall, a comparative analysis of carrier dynamics in films comprising different matrix morphologies as well as several types of interlinking ligands has shown that the matrix encapsulation strategy may ultimately provide a conceptually better scheme for the surface passivation of embedded nanoparticles, which helps to suppress carrier scattering.

RESULTS AND DISCUSSION

To determine the rate of charge trapping in nanocrystal films, the dynamics of this process should be uniquely distinguished from other mechanisms of exciton decay, which include charge tunneling between adjacent nanoparticles, variable range hopping (VRH),[56] and the resonant energy transfer to a dark state.[57] All of these processes result in the dissociation of nanocrystal excitons causing a corresponding drop in the FL lifetime. Notably, the exciton binding energy is relatively small compared to the thermal energy of photoinduced charges, such that the carrier ionization time is approximately the same as the time of carrier tunneling or hopping. Consequently, the FL lifetime of PbS nanocrystals can be used to determine the cumulative rate of carrier removal from the excited state. Namely, the rate of fluorescence intensity decay of nanocrystals in a solid can be expressed as

$$\begin{aligned}\Gamma_{\text{FL decay}} &= \Gamma_{\text{rad}} + \Gamma_{\text{nonrad}} \\ &= \Gamma_{\text{rad}} + \Gamma_{\text{trapping}} + \Gamma_{\text{tunneling}} + \Gamma_{\text{VRH}} + \Gamma_{\text{energy transfer}}\end{aligned} \quad (1)$$

When the electrical coupling between neighboring nanocrystals is strong, the radiative decay rate becomes negligibly small compared to the rate of carrier removal *via* transfer processes, $\Gamma_{\text{rad}} \ll \Gamma_{\text{nonrad}}$. As a result, the band edge emission from individual NCs in the film is suppressed, and the FL lifetime, $\tau_{\text{FL}} = 1/\Gamma_{\text{FL decay}}$, becomes roughly equal to the exciton decay time *via* nonradiative processes, $\tau_{\text{FL}} \approx \tau_{\text{nonrad}} = 1/(\Gamma_{\text{trapping}} + \Gamma_{\text{tunneling}} + \Gamma_{\text{VRH}} + \Gamma_{\text{energy transfer}})$. On the contrary, for weakly coupled nanocrystal films (Mott insulator regime), the energy and charge transfer processes between PbS NCs in the film have a relatively low probability. This causes the contribution of the radiative decay into the total exciton decay rate to become more significant, which is manifested by the enhancement of the fluorescence lifetime and the corresponding increase in the emission quantum yield of nanocrystal films featuring large interparticle distances.[54]

According to eq 1, one can determine the averaged charge trapping time for the case of nanocrystal films with strong electrical coupling between neighboring nanoparticles ($\Gamma_{\text{rad}} \ll \Gamma_{\text{nonrad}}$), provided that the remaining processes of exciton dissociation are suppressed, $\Gamma_{\text{tunneling}} + \Gamma_{\text{VRH}} + \Gamma_{\text{energy transfer}} \rightarrow 0$. This scenario can be artificially created if wide band gap ZnS semiconductor nanocrystals are introduced into the film of PbS nanoparticles, as shown in Figure 1. The addition of ZnS dots increases the interparticle separation between PbS NCs, which causes the reduction of tunneling, short-range hopping, and energy transfer rates. Indeed, the amplitude of the energy transfer process is inversely proportional to the fourth power of the interparticle distance and will be significantly diminished when PbS NCs become surrounded by ZnS NCs. At the same wide band gap, ZnS will provide a substantial potential barrier to conduction and valence band charges in the film, such that PbS-to-PbS tunneling is expected to be negligible, as well. Finally, the VRH process, which couples the resonant states of closely lying PbS nanocrystals will also be reduced by the presence of ZnS insulating dots. In particular, the rate of short-range hopping between the neighboring nanoparticles will clearly diminish with increasing fraction of ZnS nanocrystals in the film. The long-range hopping between the resonant states of nonneighboring dots, on the other hand, will only be partly suppressed as hopping of excited charges in resonance will still be possible across longer distances. It should be noted that the term suppression does not necessarily imply a complete eradication of a certain decay pathway but rather a significant reduction of its rate.

To understand whether the addition of ZnS NCs to PbS NC solids can facilitate the suppression of charge and energy transfer between adjacent PbS nanoparticles, we have fabricated several mixed films featuring different ratios of ZnS to PbS NCs and measured the corresponding lifetimes of the fluorescence intensity decay. A previously developed, semiconductor matrix-encapsulated nanocrystal arrays (SMENA) approach[53] was used to incorporate both ZnS to PbS NCs into ZnS matrices (see Figure 2a). To this end, PbS NCs capped with a shell of CdS semiconductor (see Supporting Information Figure SF1 for absorbance data)[58] were mixed with ZnS NCs, spin-coated onto a glass substrate, subjected to a ligand exchange with MPA

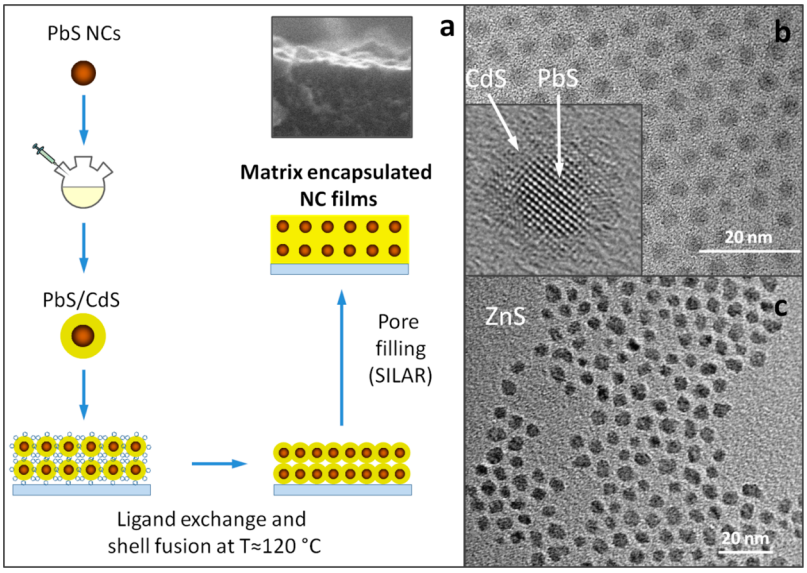

Figure 2. (a) Illustration of the general strategy for encapsulation of colloidal nanocrystals into semiconductor matrices. (b,c) Characteristic TEM images of PbS/CdS core/shell and ZnS NCs used as nanoparticle precursors during film assembly.

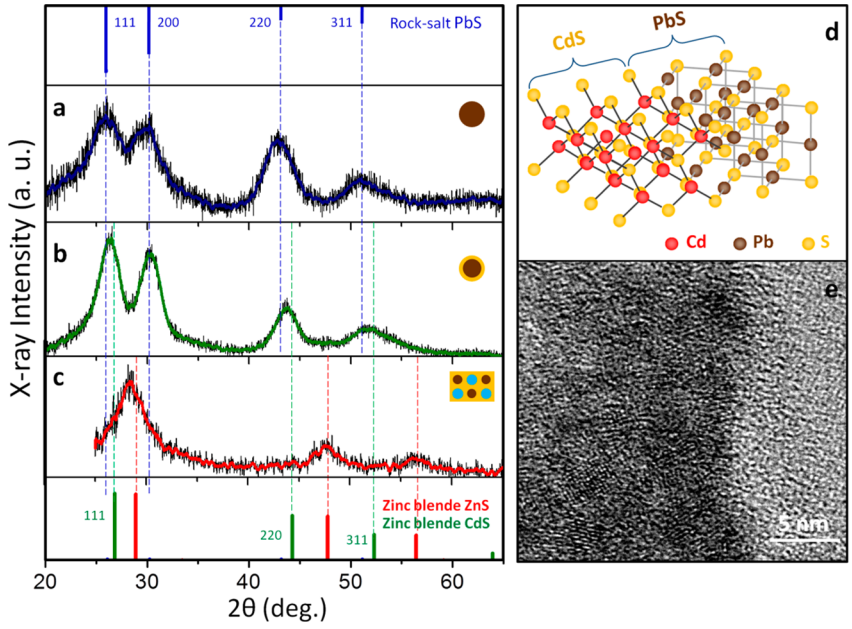

Figure 3. X-ray powder diffraction spectra of NC films corresponding to several stages of film development. (a) XRD spectrum of 4.0 nm PbS NCs, showing characteristic Bragg peaks of rock-salt PbS crystal phase. (b) XRD spectrum of fused PbS/CdS core/shell NCs. (c) XRD spectrum of fused PbS/CdS and ZnS nanocrystals prior to the pore in-filling procedure. (d) Illustration of lattice matching at the interface of rock-salt PbS and zinc blende CdS crystalline phases. (e) Fragment of the PbS/CdS SMENA solid fabricated *via* crystallographic fusion of PbS/CdS NCs.

molecules, and baked at approximately 120 °C. The heating step resulted in a removal of the organic phase, as was confirmed by FTIR measurements, and simultaneous fusion of the neighboring shells. The pores of the resulting matrix were then in-filled with additional ZnS using the successive ionic layer adsorption and reaction (SILAR)[59] approach. The XRD spectrum in Figure 3 shows the diffraction patterns of the PbS NCs (Figure 3a), PbS NCs placed within a CdS matrix (Figure 3b), and a mixture of PbS and ZnS nanoparticles placed within a CdS matrix (Figure 3c). Films featuring both PbS and ZnS nanocrystals showed a distinguishable band edge emission of PbS NCs while exhibiting a characteristic ZnS diffraction pattern, indicating that both types of nanoparticles were successfully encapsulated into matrices. A TEM image of CdS-imbedded PbS nanocrystals is shown in Figure 3e.

Figure 4b illustrates the effect of the increasing fraction of ZnS nanoparticles in CdS-encapsulated PbS/ZnS NC films (fabricated without a pore in-filling step) on the ensuing PbS exciton lifetime. Prior to the addition of ZnS, the FL lifetime of band edge excitons

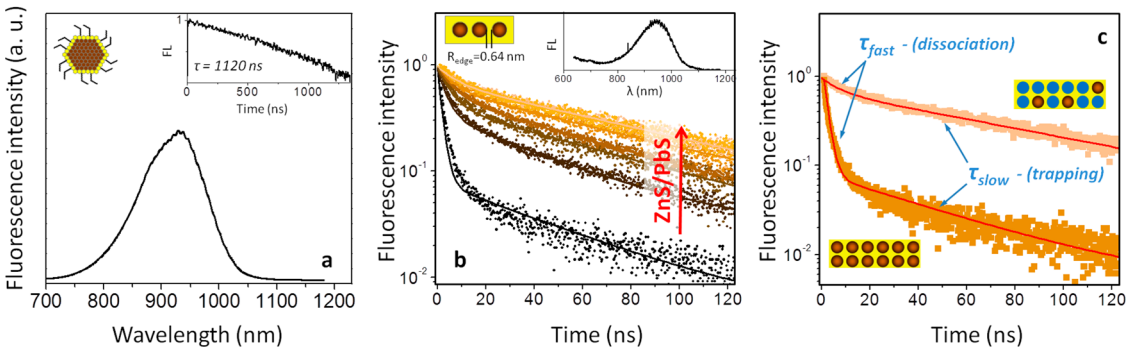

Figure 4. (a) Steady-state emission and fluorescence intensity decay (inset) of PbS/CdS core/shell NCs in solution (ΔH_{CdS} = 0.32 nm). (b) Fluorescence intensity decay of PbS NCs embedded into CdS matrices (R_{edge} = 0.64 nm) as a function of the increasing fraction of ZnS nanoparticles in the film. Steady-state emission of mixed PbS/ZnS nanoparticle films in ZnS matrices is shown in the inset. (c) Biexponential fit of the FL intensity decay curves showing the fast and slow components, which were attributed to exciton dissociation and charge trapping processes, respectively.

in PbS NCs exhibited a biexponential decay (Figure 4b, black curve) with fast and slow components being approximately equal to 1.6 and 50 ns, respectively. A relatively short lifetime of the fast exponent in this case is attributed to a high rate of interparticle charge and energy transfer, which causes a rapid dissociation of bound electron−hole pairs resulting in the suppression of the band gap emission. With the increasing fraction of insulating ZnS NCs in the matrix, such dissociation process becomes inhibited, causing the fast component of the PbS exciton decay to increase sharply from 1.6 to 8.9 ns (Figures 4b and 5a). The slow decay component also grows with the increasing fraction of ZnS NCs but at a much slower pace changing from 50 ns for no-ZnS films to 87 ns for ZnS-rich solids. Both the fast and the slow exponents eventually saturate, exhibiting no significant changes upon further addition of ZnS.

The origin of the fast and slow components in the FL decay of PbS excitons is revealed by their characteristic dependence on the fraction of insulating ZnS nanocrystals in the film. To explain a substantial growth of the fast decay component in ZnS-saturated films, we recall that prior to the addition of ZnS, the edge-to-edge distance between neighboring PbS NCs, R_{edge} = 2 × 0.32 nm = 0.64 nm, is sufficiently short to promote tunneling of charges. In fact, this value is typical of photoconducting NC devices, such as solar cells,[53] while larger R_{edge} values, especially in excess of 2 nm, tend to render the solids insulating. When the fraction of ZnS NCs in the film is high, PbS NCs become fully surrounded by wide band gap ZnS nanoparticles, such that the minimum R_{edge} distance between PbS NCs reaches $R_{edge} = 2\Delta H + d_{ZnS}$, where ΔH is the CdS shell thickness, and d_{ZnS} is an average diameter of ZnS NCs (d = 4.6 nm). Consequently, upon saturation of the PbS/CdS matrix with ZnS, R_{edge} increases from 0.64 nm to at least 5.2 nm, causing a dramatic suppression of the PbS-to-PbS transport. Considering that PbS NCs are well spaced by the ZnS insulating barrier, we propose

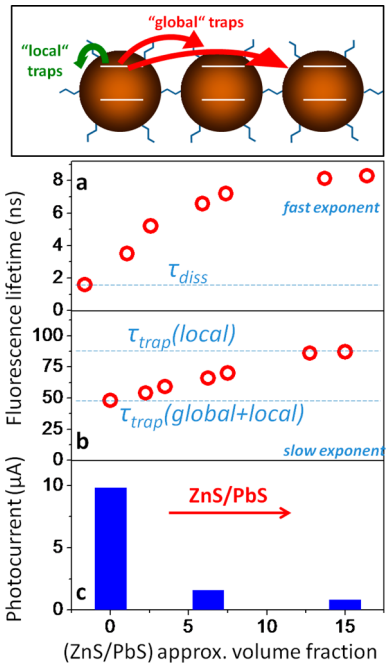

Figure 5. Summary of the FL decay dynamics for CdS-embedded PbS NC solids. (a) Evolution of the fast FL decay component with increasing fraction of ZnS NCs in the film. The exciton dissociation time is given by the FL lifetime of no-ZnS PbS films. (b) Evolution of the slow FL decay component with increasing fraction of ZnS NCs in the film. The ZnS-saturated FL lifetime is approximately equal to the characteristic time of charge trapping on "local" defects, while the FL lifetime no-ZnS solids indicate the time of carrier trapping on both "global" and "local" defect states. (c) Photoconductivity measurements performed on the same films as in parts (a) and (b). Au/Pd electrodes were sputtered through a shadow mask.

that when the saturation fraction of ZnS NCs is reached, all interparticle transfer processes, including tunneling, short-range hopping, and resonant energy transfer, are suppressed. This behavior is consistent with the results of photocurrent measurements performed on the same nanoparticle films, which confirm that increasing concentration of ZnS "insulators" in the film causes the suppression of the photoinduced current

(see Figure 5c). Based on these observations, the fast component of the FL decay was assigned to exciton dissociation processes (as illustrated in Figure 4c), which result in the energy and charge transfer between neighboring PbS nanocrystals.

As stated above, the suppression of exciton dissociation pathways in ZnS-saturated PbS NC solids ($R_{edge} \approx$ 0.64 nm) results in the inhibition of the fast decay component and the corresponding reduction of the film photoconductivity. Nevertheless, the slow component of the FL decay undergoes only small changes, growing from 50 to 87 ns (Figure 5b). In the meantime, the lifetime of the slow decay component in ZnS-saturated PbS NC films is still considerably shorter than the radiative lifetime of 3.3 nm PbS/CdS core/shell NCs in solution ($\tau \geq 1120$ ns), which lower bound was estimated from the emission lifetime of these nanoparticles in chloroform (Figure 4a inset). A 20-fold difference between τ_{rad} and $\tau_{FL,slow}$ values points toward the existence of yet another nonradiative decay channel, which is largely independent of the interparticle distance. According to eq 1, this process is trapping of electrical charges on nanocrystal surfaces. Since all transfer processes are suppressed, the characteristic time scale for such carrier trapping becomes approximately equal to the measured FL lifetime of the slow component in ZnS-saturated PbS NC films, $\tau_{trapping} \approx \tau_{FL,slow} = 87$ ns.

The character of trapping processes in PbS solids is further elucidated through the unique dependence of the slow component of the FL decay on the fraction of ZnS nanocrystals in the film. According to Figure 5b, $\tau_{FL,slow}$ is growing from 50 to 87 ns, indicating that some of the trapping events become inhibited by ZnS domains, while others are independent of the ZnS "insulation". To explain these phenomena, we would like to introduce the concept of local and global traps, as illustrated in the scheme of Figure 5. Namely, when the photoinduced charges become trapped within the same PbS dot (local traps), the rate of trapping will not be affected by the increasing fraction of ZnS NCs; meanwhile, when trapping occurs on the surface of a neighboring dot and therefore requires carrier transport (global trap), the rate of this process will be dramatically reduced when ZnS is added. Consequently, the slow component of the FL decay in pure PbS films (no-ZnS) reflects a combination of local and grobal traps (see Figure 5b), while carrier decay in ZnS-saturated films is determined primarily by the local traps.

To confirm that global traps do exist in PbS films, we have looked into the FL decay of OA-capped PbS NC solids. It is reasonable to expect that upon transferring of OA-capped PbS NCs from solution into a solid form new traps will not be created. Consequently, if the slow component of the FL decay was determined only by the local traps, it would remain constant for both the solution and the solid forms. However, our measurements (see Figure SF2) show that there is at least a 30% drop in the FL lifetime of PbS excitons when nanocrystals are deposited into films. In contrast to PbS NC solutions where FL lifetime appears to be single-exponential, the FL decay curve of a PbS solid picks up a fast (dissociation) component with the slow component decreasing from 380 to 290 ns. Consequently, some global trapping between neighboring dots must be taking place. This process is clearly inhibited for dots in solution but becomes feasible for solid-bound nanocrystals even if new traps are not created.

While the evolution of the fast and the slow components in the FL decay of PbS/ZnS solids appears to be consistent with proposed assignments of dissociation and trapping mechanisms, the lack of the FL lifetime saturation in ZnS-rich films needs further explanation. Namely, when the volume fraction of ZnS nanoparticles in the ZnS/PbS film reaches the 10−15 range, one can expect that all charge and energy transfer processes should be inhibited. Nevertheless, the fast component is still present in the decay trace of ZnS-dominated PbS/ZnS films (see Figure 4b,c). Furthermore, the photoconductivity of nanoparticle solids does not go to zero completely, even when all PbS nanocrystals are presumably surrounded by insulating ZnS nanoparticles (see Figure 5c). To explain this phenomenon, we propose the existence of the long-range hopping mechanism, which couples non-neighboring PbS dots in resonance. Indeed, if the photoinduced charge transfer can occur across long-range distances, even high volume fractions of ZnS NCs may not be sufficient to suppress the exciton dissociation, as evident by the lingering fast component in Figure 4b. Similarly, the existence of long-range hopping can explain the nonvanishing carrier conductivity in the film, evidenced as the residual photocurrent in ZnS-saturated solids. Temperature-dependent photoluminescence studies can be performed in the future to confirm the VRH contribution to the charge transport in films comprising large ZnS/PbS volume fractions.

To find further evidence supporting the proposed assignments of fast and slow FL decay components to the processes of dissociation and trapping, we have looked into the dynamics of FL decay in weakly coupled PbS solids. To this end, the R_{edge} distance in the PbS/CdS matrix was increased from 0.64 to 2.7 nm, by augmenting the thickness of the CdS layer in PbS/CdS film precursor nanoparticles to 1.3 nm. Since the CdS layer provides a small potential barrier to both types of charge carriers (see Figure SF3), the processes of exciton dissociation (*e.g.*, *via* PbS-to-PbS charge transfer) and charge trapping on surface states of core/shell nanoparticles are expected to be inversely proportional to the thickness of the shell. For instance, if we assume that tunneling of photoinduced carriers from PbS cores to the surface of the shell is the main

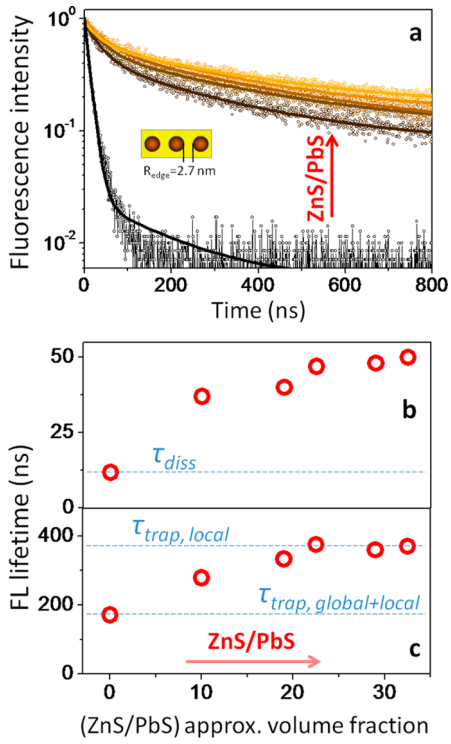

Figure 6. (a) Fluorescence intensity decay of weakly coupled PbS NCs embedded into CdS matrices (R_{edge} = 2.7 nm) as a function of the increasing fraction of ZnS nanoparticles in the film. (b) Evolution of the fast FL decay component with increasing fraction of ZnS NCs in the film. The exciton dissociation time is given by the FL lifetime of no-ZnS PbS films. (c) Evolution of the slow FL decay component with increasing fraction of ZnS NCs in the film. The ZnS-saturated FL lifetime is approximately equal to the characteristic time of charge trapping on "local" defects, while the FL lifetime no-ZnS solids indicate the time of carrier trapping on both "global" and "local" defect states.

mechanism of carrier trapping, then the probability of this process can be estimated using Wentzel–Kramers–Brillouin (WKB) approximation[60] as a single-exponential dependence on the shell thickness, $\Gamma_{thick}/\Gamma_{thin} = \exp(-\Delta H_{thick})/\exp(-\Delta H_{thin})$, where Γ is the charge trapping rate. In principle, lattice defects forming along core/shell interfaces can also contribute into the exciton dissociation, but the characteristic time associated with such a de-excitation process is much greater than that of other trapping mechanisms. Indeed, the lower limit of the interfacial trapping time is given by the FL lifetime of core/shell NCs in solutions (τ = 1120 μs, Figure 4a), which exceeds the exciton lifetime of film-bound PbS NCs by 2 orders of magnitude. Such a low probability of charge trapping along PbS/CdS interfaces is expected due to nearly matched lattice parameters of rock-salt PbS and zinc blende CdS crystal phases (strain $\approx$ 1.7%; see Figure 3d).

Figure 6 illustrates the changes in the FL lifetime of CdS-encapsulated PbS NC solids ($R_{edge} \approx$ 2.7 nm) with increasing fraction of ZnS nanoparticles in the film. Prior to the addition of ZnS NCs, the fast component of the FL decay, limited primarily by PbS-to-PbS excitation transfer processes (see eq 1), was found to be 11.6 ns. Notably, this value is substantially greater than the corresponding FL lifetime of strongly coupled PbS NC films featuring R_{edge} = 0.64 nm. The positive correlation between the FL lifetime of PbS excitons and R_{edge} distance in the matrix (prior to the addition of ZnS) is attributed to the suppressed tunneling, short-range hopping, and energy transfer across an increased layer of the CdS potential barrier (R_{edge} = 0.64 nm → 2.7 nm). According to WKB approximation, the expected reduction in the exciton dissociation rate (fast component) is exponential with R_{edge}, exp(−0.64)/exp(−2.7) = 7.8, which is close to the observed lifetime ratio, $\tau_{2.7\ nm}/\tau_{0.64\ nm}$ = 11.6/1.6 = 7.25. When ZnS is introduced into the film, charge transfer processes become further suppressed, causing the fast lifetime component to continue climbing in value while diminishing in amplitude (see Figure 6b). Similarly to the case of R_{edge} = 0.64 nm, the fast exponent of the FL decay in PbS films with R_{edge} = 2.7 nm eventually becomes overwhelmed by the slow component, which represents charge trapping processes. The slow exponent eventually saturates with the continuous increase of the ZnS volume fraction in the film, ultimately reaching $\tau_{FL,slow}$ = 370 ns. Since charge and energy transfer processes are strongly suppressed for this film morphology, trapping of charges on local surface traps becomes the main mechanism of exciton dissociation, $\tau_{trapping}$(local) $\approx$ $\tau_{FL,slow}$ = 370 ns. The observed trapping time for weakly coupled PbS NC films is approximately 370/87 = 4.25 times greater than the corresponding value of strongly coupled PbS NC solids (R_{edge} = 0.64 nm). The observed reduction of the trapping rate falls somewhat short of the WKB estimates, exp(−0.64)/exp(−2.7) = 7.8, which indicates that additional relaxation pathways may begin to play a role when the FL lifetime extends into hundreds of nanoseconds.

In-filling of interparticle "pores" in matrix-encapsulated nanocrystal films can result in the further suppression of charge trapping on surface states. Since interfaces of PbS/CdS core/shell NCs are generally defect-free (Γ_{trap}(interfacial defects) < 1/450 ns), we expect that the primary contribution into carrier trapping must come from scattering of photoinduced charges on unpassivated surfaces of the CdS matrix. To reduce the probability of such surface trapping, the width of the potential barrier separating PbS-localized carriers from surface states could be enhanced, for instance, by depositing additional layers of the CdS or ZnS semiconductor on surfaces of interfused nanocrystals. Here, to understand the effect of such surface treatment on the carrier dynamics, several monolayers of ZnS have been deposited onto both no-ZnS and ZnS-saturated PbS NC matrix (R_{edge} = 0.64 nm) *via* SILAR methodology. In the case of no-ZnS films where carrier trapping occurs both locally and globally, the

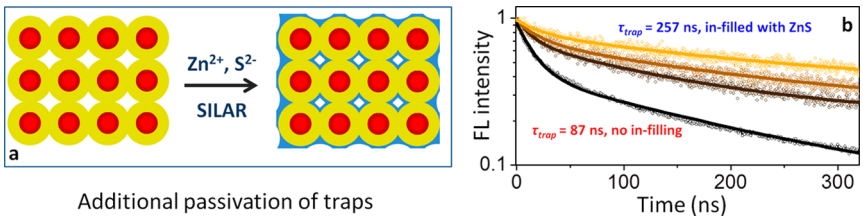

Figure 7. (a) Illustration of the in-filling strategy based on SILAR deposition of ZnS. (b) Effect of SILAR treatment on the fluorescence intensity decay of CdS-encapsulated PbS/ZnS nanoparticle film, with suppressed charge/energy transfer processes. The enhanced FL lifetime of pore in-filled films is attributed to the reduction in the charge trapping rate.

addition of six ZnS monolayers leads to a 35% increase in the FL lifetime of the slow component (Figure SF4). Such a moderate enhancement of the trapping time can be attributed to the existence of global traps which originate from below the surface layer and thus cannot be filled. In the case of ZnS-saturated solids featuring only local traps (situated on the same dot), the SILAR treatment results in a more substantial 3-fold increase in the slow decay component, $\tau_{FL,slow}$ = 87 → 257 ns (see Figure 7b), indicating that atomic layer deposition effectively passivates surface traps. Notably, the fast decay component in ZnS-saturated PbS films was not fully inhibited by the in-filling step. The continuing presence of this decay component is corroborated by the proposed long-range hopping mechanism, which rate is primarily determined by the interparticle distance rather than surface passivation.

We now turn our attention to ligand-linked PbS NC solids, for which nanoparticle surfaces are passivated by short-chain molecules. Here, by varying the fraction of ZnS nanocrystals in a film, we seek to determine whether ligand-linked and CdS-encapsulated NC solids exhibit different rates of exciton dissociation and charge trapping, a question which is directly related to the material's electrical performance. For this study, we have narrowed our choice of ligands down to three representative molecules, which include MPA, 1,2-ethanedithiol (EDT), and a hybrid combination of MPA/Cl ligands. All of these materials have been previously employed as charge conducting surfactants in best-performing nanocrystal devices.[27,61]

We start our analysis with MPA-linked PbS nanoparticle films, fabricated *via* the spin-coating process according to standard protocols.[61] The addition of ZnS NCs into MPA-linked PbS NC film (d = 3.2 nm) results in the suppression of the charge transfer processes much like it was observed for matrix-encapsulated NC solids. According to Figure 8e,h, the FL lifetime of the fast decay component in all-PbS films prior to the addition of ZnS was 1.04 ns, while the lifetime of oleic-acid-passivated PbS NCs in nonpolar solvents is 480 ns. The reduction in the emission lifetime of PbS excitons accompanying the transfer of PbS nanoparticles from solution into a solid film is again attributed to the combination of competing exciton dissociation processes, which include resonant charge transfer, resonant energy transfer to a dark state, hopping, and charge trapping. In theory, the transfer of photoinduced holes to MPA ligands can also contribute to carrier ionization. The rate of the latter process, however, is too slow to compete with other energy and charge transfer mechanisms since the FL lifetime of 11-mercaptoundecanoic acid (MUA)-capped PbS dots in water/methanol solution is 220 ns (see Figure SF5).

Increasing the fraction of ZnS nanocrystals in MPA-linked PbS NC films results in the enhancement of the fast FL decay component, which reflects the suppression of charge transfer processes between neighboring PbS dots. The slow decay component, associated with charge trapping on NC surfaces, grows from τ = 35 ns for no-ZnS films (global + local traps) to a saturation level of τ_{trap}^{MPA} = 60.5 ns (averaged over three different films), which corresponds to carrier decay on local traps only. Notably, this later value is approximately 4 times as short as $\tau_{trap,local}$ of matrix-encapsulated PbS films in-filled with ZnS, τ_{trap}^{CdS} = 257 ns. Similar results were obtained for EDT-linked films (see Table 1), where the charge trapping time has grown from 25 to 45 ns.

One of the best-performing solar cell devices utilizing ligand-linked NC films was recently made by employing a combination of MPA and halide anion ligands. Halide atoms, such as chlorine, are compact enough to infiltrate difficult-to-access sites of nanocrystals, providing better surface passivation, leading to the reduced density of midgap trap states.[27] Here, to understand the role of halide passivation, we have measured the exciton dissociation dynamics in PbS NC solids comprising hybrid MPA/Cl ligands (Figure 8f,j). The addition of chlorine ligands to the surface of PbS NCs during the solution growth step has resulted in a 10% enhancement of the FL lifetime (Figure 8c, inset) and the associated 20−25% increase in the FL quantum yield. In a solid form, MPA/Cl-passivated PbS NCs showed an expected biexponential character of the FL decay with fast and slow components being equal to 3.1 and 30 ns, respectively, for no-ZnS films. With the addition of ZnS nanoparticles, the latter lifetime increased to 193 ns (Figure 8f), reflecting an approximate time of carrier decay on local traps. Expectedly, the use of chlorine capping resulted in the reduced rate of charge trapping on NC surfaces (τ_{trap} = 193 ns) compared to MPA-linked PbS films, which agrees well

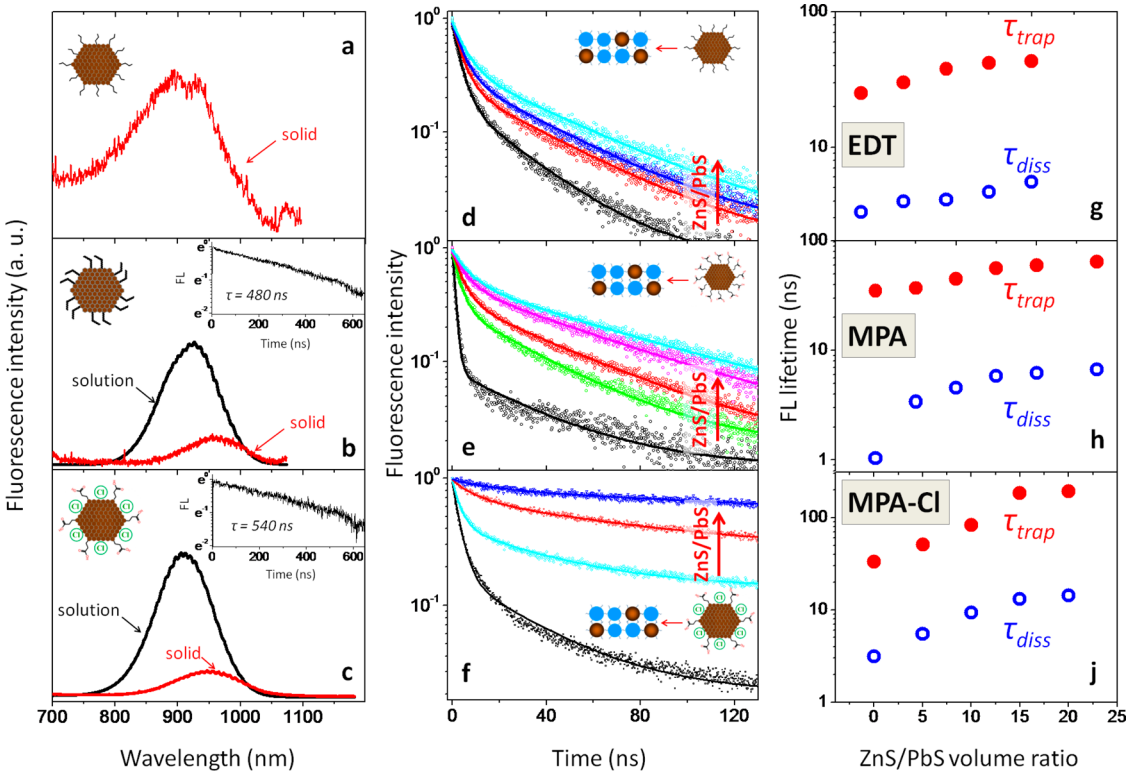

Figure 8. (a–c) Steady-state emission of PbS NCs passivated with EDT (a), MPA (b), and MPA/Cl (c) in different environments, as indicated in the figure. The insets in (b) and (c) show the corresponding FL intensity decay for nanocrystals in solution. (d–f) Fluorescence intensity decay of PbS NC films, cross-linked with EDT (d), MPA (e), and MPA/Cl (f) molecules as a function of increasing fractions of ZnS nanoparticles in the film. (g–j) Dependence of the PbS exciton lifetimes (fast and slow components) on the concentration of ZnS nanoparticles for the three types of molecular linkers.

TABLE 1. FL Lifetime Data and Derived Transport Characteristics of Matrix-Encapsulated and Ligand-Linked PbS Nanocrystal solids

		τ_{diss} (ns)	τ_{trap} (ns) global+local	τ_{trap} (ns) local		$l_{diffusion}$ (nm)	
type of NC film	number of films tested	τ_{fast}; no ZnS	τ_{slow}; no ZnS	τ_{slow}; ZnS-sat	μ ($cm^2/V/s$) (eq[4])	glob+loc	local
CdS-encapsulated PbS NCs (R_{edge} = 0.64 nm)	2	1.6	65 (with SILAR)	257.0 (with SILAR)	0.57×10^{-3}	9.8	20.1
CdS-encapsulated PbS NCs (R_{edge} = 2.7 nm)	2	11.6	171	370	1.8×10^{-4}	9.0	13.3
MPA-linked PbS NCs	3	1.04	35	60.5	0.9×10^{-3}	9.0	11.8
EDT-linked PbS NCs	1	3.4	25	45	0.2×10^{-3}	4.2	5.7
hybrid (MPA/Cl)- linked PbS NCs	1	3.1	33	193	0.3×10^{-3}	5.1	12.3

with the predictions of a recently developed diffusion model.[62] The use of hybrid ligands, however, has yielded a longer exciton dissociation time (Figure 8f,j), which was attributed to the existence of the surface potential barrier associated with a chlorine layer on PbS NCs. A somewhat surprising outcome of these measurements was the observation of similar (no-ZnS) decay times for MPA-only and MPA/Cl-passivated PbS films. This could be ascribed to a relatively high density of rare deep traps[62] in MPA/Cl films, which promote global trapping of photoinduced charges.

The comparison of the FL lifetimes between matrix-encapsulated and ligand-linked PbS NC solids featuring similar interparticle distances reveals an important trend: trapping of photoinduced charges in CdS-encapsulated PbS NC matrices is reduced in comparison with ligand-linked PbS films. To get a quantitative interpretation of the observed charge transport characteristics, we recall that for a typical p-n junction, carrier transport relies on drift in the depletion region and diffusion elsewhere. If the minority carrier lifetime, τ, is known, the characteristic lengths of drift and diffusion can be estimated using the following equations:

$$l_{drift} = \mu E\tau;\ l_{diffusion} = \sqrt{D\tau} \qquad (2)$$

where μ is the charge carrier mobility, D is the diffusion coefficient, and E is the electric field in the drift region. Since charge trapping is the primary process of carrier

scattering in both types of NC films, we assume that minority carrier lifetime is approximately the same as the trapping time $\tau \approx \tau_{trap}$. In order to estimate l_{drift} and l_{diff} values for investigated films, charge carrier mobility, μ, and the diffusion coefficient, D, have to be determined first. Fortunately, an estimate of μ and D for a nanocrystal solid in the *hopping transport regime* can be obtained from the Einstein's relation between mobility and diffusion:

$$\mu = \frac{ed^2}{6kT}\frac{1}{\tau};\ D = \frac{\mu kT}{e} \qquad (3)$$

where d is the center-to-center distance between PbS NCs in a film, and $(1/\tau)$ represents the cumulative rate of carrier diffusion processes, including charge transfer, energy transfer to a dark state, and hopping. The approximation is based on the assumption that carrier diffusion is accompanied by the transfer of the excitation energy to a neighboring nanocrystal. Therefore, the band transport regime cannot be described using this approach, and the resulting μ_{diff} represents diffusion-limited charge carrier mobility in a nearest-neighbor hopping approximation. We note that μ_{diff} is different from the field-effect transistor (FET) mobility, μ_{FET}, which characterizes solids with an altered position of the Fermi level, as controlled by the gate voltage. In order to estimate μ_{diff} for investigated film architectures, the carrier diffusion rate $(1/\tau_{diff})$ has to be determined first. Here, this was achieved by measuring the fast component of the FL decay in PbS-only films. Namely, since all charge transfer processes are allowed in the absence of ZnS NCs, the rate of the FL decay becomes $\Gamma_{FL\ decay} = \Gamma_{trapping} + \Gamma_{rad} + \Gamma_{diff}(\Gamma_{tunneling};\ \Gamma_{VRH};\ \Gamma_{energy\ transfer})$, where the latter term represents exciton diffusion processes characterized by the fast component in the FL decay, $\tau_{diff} \approx \tau_{ex.dissociation} = \tau_{FL,fast}$ (no ZnS). Consequently, eq 3 can be expressed as

$$\mu_{diff} = \frac{ed^2}{6kT}\frac{1}{\tau_{FL,fast}^{no\ ZnS}};\ D = \frac{\mu kT}{e} = \frac{d^2}{6\tau_{FL,fast}^{no\ ZnS}} \qquad (4)$$

Finally, the charge carrier diffusion length becomes

$$l_{diffusion} = \sqrt{D\tau_{trap}} = d \times \sqrt{\tau_{trap}/6\tau_{FL,fast}}$$
$$= d \times \sqrt{\tau_{FL,slow}/6\tau_{FL,fast}} \qquad (5)$$

where $\tau_{FL,slow}$ corresponds to the slow component of either no-ZnS (local and global traps) or ZnS-saturated (local traps only) FL lifetime in NC solids.

Table 1 summarizes the FL lifetime data for matrix-encapsulated and ligand-linked PbS NC solids. Arguably, the most significant outcome of the above comparison is the suppressed carrier trapping observed for matrix-encapsulated nanocrystal films. In particular, charge trapping rates for strongly coupled PbS/CdS films appear to be 1.5−4 times lower than for the three investigated types of ligand-linked nanoparticle solids. Cl-passivated PbS NC solids were likewise fairly efficient in inhibiting carrier trapping on "local" defects with the characteristic scattering time (τ_{trap} = 193 ns) exceeding that of MPA-only films by a factor of 3. As discussed above, this serves as indirect evidence that matrix-encapsulated and Cl-passivated NC solids exhibit comparatively low densities of surface trap states. On the other hand, the diffusion carrier mobility for all-inorganic PbS/CdS films, $\mu_{diff} = 0.57 \times 10^{-3}$ cm^2/V/s, was found to be somewhat lower than the corresponding mobility value for MPA-linked PbS solids ($\mu_{diff} = 0.9 \times 10^{-3}$ cm^2/V/s). It should be noted, however, that electrical coupling of CdS-encapsulated films, determined by the PbS-to-PbS interparticle distance, was below its previously reported maximum, which corresponds to R_{edge} = 0.5 nm. Based on the comparison of R_{edge} = 0.64 nm and R_{edge} = 2.7 nm PbS/CdS solids (lines 1 and 2 in Table 1), we conclude that R_{edge} plays a critical role in the ensuing value of μ_{diff}. Therefore, the mobility of CdS-encapsulated films can potentially be increased by using a sufficiently low R_{edge}, which promotes fast exciton dissociation yet partly preserves quantum confinement of charges. Further studies will be needed to confirm this hypothesis.

Another point that merits explanation is the nature of the calculated diffusion mobility, which was found to be at least 1 order of magnitude lower than a typical value of μ_{FET} for MPA-linked films. In this regard, we recall that within the approximation of hopping transport regime, charge carriers are presumed to be localized within individual dots, such that the mobility is determined by tunneling to the nearest unoccupied state. Meanwhile, in the case of FET measurements, the raised (or lowered) position of the Fermi level leads to the population of *overbarrier* states, which enhances the delocalization of carriers and increases the mobility.

In case of photovoltaic applications of semiconductor nanocrystals, increasing carrier mobility beyond 10^{-2} cm^2/V/s does not proportionally avail the device performance since exciton dissociation is already quite efficient.[46] The true advance can be achieved through the eradication of the carrier recombination centers, typically midgap surface traps, which would result in the enhancement of an average l_{diff} and l_{drift} in the film. This study demonstrates that trapping of charges in nanocrystal solids can be reduced if matrix encapsulation is used in lieu of the cross-linking approach. Indeed, the comparison of l_{diff} (Table 1) and l_{drift} (Table ST1) values reveals that CdS-encapsulated nanocrystal solids provide somewhat longer scatter-free travel of carriers than other types of films. The longer diffusion length for these materials indicates that a long minority carrier lifetime outweighs a relatively lower mobility of carriers in matrix-encapsulated films.

CONCLUSIONS

In conclusion, the dynamics of exciton dissociation and charge scattering processes in several types of PbS nanocrystal solids have been studied using

fluorescence lifetime spectroscopy. To determine the characteristic time scale of charge scattering for each film type, a controlled amount of "insulating" ZnS nanoparticles was introduced into the solids of PbS NCs. The presence of ZnS nanoparticles in the film causes the suppression of both energy and charge transfer processes between PbS dots, allowing carriers to decay primarily by trapping on nanocrystal surfaces. FL lifetime technique can then be employed to measure the dynamics of photoinduced charge scattering separately from other processes of charge and energy transfer. Based on the observed relaxation times, we have determined the rates of exciton dissociation and charge trapping for several types of NC films, featuring either matrix encapsulation or cross-linking assembly strategies. The observed decay rates were also used to determine the diffusion carrier mobility and scattering lengths for all film types within the hopping regime of carrier transport. Overall, matrix-encapsulated PbS NC films showed lower rate of charge trapping on surfaces and longer diffusion lengths than any type of ligand-linked PbS nanocrystal films.

EXPERIMENTAL SECTION

Chemicals. 1-Octadecene (ODE, 90% Aldrich), oleic acid (OA, 90% Aldrich), cadmium oxide (CdO, 99.99%, Aldrich), lead(II) oxide powder (PbO, 99.999% Aldrich), sodium sulfide nonanhydrate ($Na_2S \cdot 9H_2O$, 98% Alfa Aesar), sulfur (S, 99.999% Acros), ethanol (anhydrous, 95% Aldrich), hexane (anhydrous, 95% Aldrich), methanol (anhydrous, 99.8% Aldrich), toluene (anhydrous, 99.8% Aldrich), isopropyl alcohol (anhydrous, 99.8% Acros), octane (anhydrous, 99% Aldrich), 3-mercaptopropionic acid (MPA, 99% Alfa Aesar), 11-mercaptoundecanoic acid (MUA, 95% Aldrich), diethylzinc (Et_2Zn, 15 wt %, 1.1 M solution in toluene, Aldrich), bis(trimethylsilyl)sulfide ($(TMS)_2S$, Aldrich, synthetic grade), tri-*n*-octylphosphine (TOP, 97% Strem), cadmium chloride ($CdCl_2$, 99.99% Aldrich), acetone (anhydrous, Amresco, ACS grade), zinc acetate (98+% Acros), tetradecylphosphonic acid (TDPA, 97% Aldrich), 1,2-ethanedithiol (EDT, 98+% Fluka), and Triton X-100 (Alfa Aesar) were used as received without any further purification. All reactions were performed under argon atmosphere using the standard Schlenk technique. Fluorine-doped tin oxide (FTO) glass (TEC 15, 12−14 Ohm/sq) was obtained from Pilkington Glass.

Synthesis of PbS NCs. The synthesis of PbS NCs was based on the procedure reported by Hines *et al.*[63] For the growth of PbS NCs with the diameter of 3.8 nm (exciton absorption feature at 1050 nm), a mixture of 0.49 g (2 mmol) of PbO, 18 mL of ODE, and 2 mL of OA in a three-neck flask was pumped at 120 °C for 2 h. After degassing the mixture, the flask was connected to argon and heated to 135 °C. Meanwhile, 10 mL of ODE was degassed for 2 h at 120 °C, switched to argon, and cooled to room temperature. The solution of sulfur precursor in ODE was prepared by injecting 0.21 mL of $(TMS)_2S$ into the second flask with stirring for 2 min. Subsequently, the full amount of $(TMS)_2S$/ODE solution was injected into the first flask and kept at that temperature for 1 min, after which the reaction was quenched by placing the flask into a cold water bath. PbS NCs were isolated from the solution by precipitating with 50 mL of acetone and centrifugation. After centrifugation, the decantate was removed and nanocrystals were redispersed in ∼15 mL of toluene. To remove all residues, the cleaning cycle was repeated two times and final sample was redispersed in a minimal amount of hexane (4−5 mL).

Preparation of $CdCl_2$ Precursor for the Synthesis of Hybrid-Passivated PbS NCs. For the preparation of the metal-halide precursor for additional passivation of PbS NCs, 0.30 g (1.64 mmol) of $CdCl_2$ and 0.033 g (0.12 mmol) of TDPA in 5 mL of oleylamine were degassed for 18 h at 100 °C, switched to argon, and kept at 80 °C to prevent solidifying.

Synthesis of the Hybrid-Passivated PbS Nanocrystals. The hybrid-passivated PbS nanocrystals were prepared using the procedure developed by Ip *et al.*[27] The synthesis of OA-capped PbS nanocrystals was performed according to the usual protocols, as described above, followed by the additional treatment of the reaction mixture during the final cooling process. Namely, after removing the flask from the heating mantle, 1 mL of the $CdCl_2$ solution prepared in the previous step was added to the reaction mixture. When the temperature reached 30 °C, ∼50 mL of acetone was added to precipitate NCs. The reaction mixture was then centrifuged, the decantate was removed, and nanocrystals were redispersed in ∼15 mL of toluene. To remove all residues, the cleaning cycle was repeated two times and final sample was redispersed in a minimal amount of hexane (4−5 mL).

Synthesis of PbS/CdS Core/Shell NCs. PbS/CdS core/shell nanoparticles were synthesized according to the procedure from ref 58 using a cation exchange methodology. To this end, 0.5 g (3.8 mmol) of CdO was dissolved in 3 mL of OA and 9 mL of ODE under Ar at 235 °C until the solution became clear. Then, the temperature of this solution was set at 80 °C. Meanwhile, 4 mL of PbS seed nanocrystals (d = 4.2 nm) solution in hexane (concentration 10 mg/mL) was kept under argon gas flow at 75 °C for 2 min to remove excess of solvent and then was injected into the cadmium solution under vigorous stirring. The reaction mixture was kept at 75 °C for 1 min and then stopped by removing the flask from the heating mantle. The purification process included the separation of nanoparticles from the solution with ∼30 mL of ethanol, centrifugation, and dissolution of the precipitated nanocrystals in a minimal amount of hexane. The cleaning cycle was repeated two times. Under these conditions, the absorbance peak was found to blue shift by 80 nm (approximately 0.35 nm of the CdS shell). The growth of the CdS shell depended on the size of PbS NCs and the reaction time. Longer reaction times, higher temperatures, and higher ratios of OA/ODE were used to obtain a thicker shell of CdS.

To determine the shell thickness in thin-shell nanocrystals (where TEM images do not provide the sufficient accuracy), the following approach was used. First, the size of original PbS dots was determined from the position of the exciton absorption edge. The reduction in the average size of the PbS domain upon Pb^{2+} to Cd^{2+} cation exchange was determined from the new position of the PbS exciton peak. The thickness of the shell was then calculated under the assumption that the diameter of the PbS/CdS core/shell structure remained the same as the diameter of the original PbS dot.

Synthesis of ZnS Nanoparticles. In a typical procedure, 2 mL of TOP solution was degassed for 2 h at 120 °C and switched to argon. Then, 1 mL of diethyl zinc and 0.2 mL of $(TMS)_2S$ were injected separately into the reaction mixture while stirring. The solution was then cooled and stirred for 30 min at 90 °C. To avoid the solidifying of unreacted TOPO, 5 mL of butanol was added into the flask right after the injection of precursors. ZnS nanocrystals were separated from the solution by precipitation in 25 mL of acetone. After centrifugation, the decantate was removed and nanocrystals were redispersed in ∼6 mL of hexane.

Preparation of the FTO/Glass Substrate. FTO-coated glass was cut into 2.5 cm × 2.5 cm squares, then washed by hand with detergent (Alconox), and rinsed clean in deionized water. It was then sonicated in methanol, acetone, and isopropyl alcohol for 5 min in each solvent.

Fabrication of Nanocrystal Films. The deposition of ligand-linked NC films was performed under argon atmosphere inside the glovebox using standard layer-by-layer techniques.[61] All-inorganic NC films (SMENA) were fabricated according to developed procedure.[53]

To deposit a layer of all-inorganic CdS-encapsulated NC film onto the FTO/glass substrate, 5−6 drops of the PbS/CdS core/shell NC solution in hexane (concentration 10 mg/mL) was placed onto the glass until the surface was covered and then the film was spun until dry at 3000 rpm for 10 s. To replace original OA ligands with thermally degradable MPA molecules, 7−10 drops of MPA/methanol solution (ratio 1:4) was deposited on the center of the glass slide, soaked for 10 s, and spun at 3000 rpm for 10 s. After the MPA treatment, the film was washed by covering with 10 drops of methanol and spinning the slide for 10 s, followed by rinsing with octane in the same manner. Upon the deposition of two layers, the films were annealed at 120−140 °C for 15 min. A total of 6−7 layers was deposited. To fabricate all-inorganic films with additional ZnS NCs, the initial solution of PbS/CdS NCs was mixed with the ZnS solution in ratios, which were calculated by dividing the optical density of ZnS colloidal precursor (at $\lambda = 270$ nm) by that of PbS/CdS NCs (at $\lambda_{ex} \approx 850-900$ nm).

MPA-linked PbS NC films were deposited using a layer-by-layer spin-coating process under an argon atmosphere. For each layer, the solution of PbS NCs in hexane (concentration 20 mg/mL) was deposited on the glass substrate and span at 3000 rpm for 10 s. Subsequently, 7−10 drops of MPA/methanol solution (ratio 1:4) was deposited on the center of the glass slide, soaked for 10 s, and spun at 3000 rpm for 10 s. The total amount of layers was varied from 6 to 10. Ratios of PbS with ZnS were calculated by dividing the optical density of ZnS colloidal precursor at the center of the exciton absorption future (at $\lambda = 270$ nm) by that of PbS NCs.

The fabrication of ethanedithiol (EDT)-linked NC films was performed using a dip-coating technique. After the deposition of 5−7 drops of PbS NCs onto FTO/glass substrate, followed by spinning at 3000 rpm for 10 s, the film was immersed into 0.1 M EDT solution in acetonitrile for 1 min, dried, and washed with 10 drops of acetonitrile. Overall, 7−10 cycles were required to fabricate a film with EDT-cross-linked PbS NCs and PbS with ZnS NCs. Ratios of PbS with ZnS for the mixed films were calculated the same way as in the case of MPA-linked films.

In-Filling of SMENA Pores with ZnS. For the pore-filling process, the SILAR method was applied.[59] Briefly, the deposition of the additional layer of the wide band gap ZnS was conducted by the sequential soaking of the annealed, all-inorganic NCs film in the methanol solutions containing Zn and S precursors. For this purpose, the zinc bath was prepared by dissolution of 0.10 g of zinc acetate in 20 mL of methanol and the sulfur bath by placing 0.098 g of $Na_2S \cdot 9H_2O$ in 20 mL of methanol. One SILAR cycle included a soaking of the film in the zinc bath for 1 min, then rinsing the film with methanol for 1 min, then soaking it in the sulfur bath for 1 min with sequential washing in methanol. A total of 2−10 cycles of pore-filling process was applied for all-inorganic films with longest lifetime. The films were then annealed at 150 °C for 15 min.

Characterization. Absorbance spectra were recorded using CARY 50 scan and Shimadzu UV-3600 UV−vis−NIR spectrophotometers. Photoluminescence spectra were recorded using a Jobin Yvon Fluorolog FL3-11 fluorescence spectrophotometer. High-resolution transmission electron microscopy (HR-TEM) measurements were carried out using JEOL 3011UHR and 2010 transmission electron microscopes, operated at 300 and 200 kV, respectively. To prepare a TEM sample, a small amount of NC film was scraped, dispersed in toluene by sonication, dropped onto a carbon-coated copper grid, and allowed to dry in air. X-ray powder diffraction (XRD) measurements were carried out on a Scintag XDS-2000 X-ray powder diffractometer. FL lifetime measurements were performed using a time-correlated single-photon counting setup utilizing SPC-630 single-photon counting PCI card (Becker & Hickle GmbH), picosecond diode laser operating at 400 nm, as an excitation source (Picoquant), an id50 avalanche photodiode (Quantique), and long pass filters on 400, 532, and 750 nm.

Conflict of Interest: The authors declare no competing financial interest.

Acknowledgment. We gratefully acknowledge OBOR "Material Networks" program and NSF Awards CHE-1112227 and CBET-1236355 for financial support.

Supporting Information Available: Additional images. This material is available free of charge *via* the Internet at http://pubs.acs.org.

REFERENCES AND NOTES

1. Murray, C. B.; Nirmal, M.; Norris, D. J.; Bawendi, M. Synthesis and Structural Characterization of II−VI Semiconductor Nanocrystallites (Quantum Dots). *G. Z. Phys. D: At. Mol., Clusters* **1993**, *26*, S231–S233.
2. Beard, M. C. Multiple Exciton Generation in Semiconductor Quantum Dots. *J. Phys. Chem. Lett.* **2011**, *2*, 1282–1288.
3. Pal, B. N.; Ghosh, Y.; Brovelli, S.; Laocharoensuk, R.; Klimov, V. I.; Hollingsworth, J.; Htoon, H. 'Giant' CdSe/CdS Core/Shell Nanocrystal Quantum Dots as Efficient Electroluminescent Materials: Strong Influence of Shell Thickness on Light-Emitting Diode Performance. *Nano Lett.* **2012**, *12*, 331–336.
4. Kramer, I. J.; Levina, L.; Debnath, R.; Zhitomirsky, D.; Sargent, E. H. Solar Cells Using Quantum Funnels. *Nano Lett.* **2011**, *11*, 3701–3706.
5. Klimov, V. I.; Mikhailovsky, A. A.; Xu, S.; Malko, A.; Hollingsworth, J. A.; Leatherdale, C. A.; Eisler, H.; Bawendi, M. G. Optical Gain and Stimulated Emission in Nanocrystal Quantum Dots. *Science* **2000**, *290*, 314–317.
6. Klimov, V. I. Mechanisms for Photogeneration and Recombination of Multiexcitons in Semiconductor Nanocrystals: Implications for Lasing and Solar Energy Conversion. *J. Phys. Chem. B* **2006**, *110*, 16827–16845.
7. Klimov, V. I.; Ivanov, S. A.; Nanda, J.; Achermann, M.; Bezel, I.; McGuire, J. A.; Piryatinski, A. Single-Exciton Optical Gain in Semiconductor Nanocrystals. *Nature* **2007**, *447*, 441–446.
8. Hillhouse, H. W.; Beard, M. C. Solar Cells from Colloidal Nanocrystals: Fundamentals, Materials, Devices, and Economics. *Curr. Opin. Colloid Interface Sci.* **2009**, *14*, 245–259.
9. Huynh, W. U.; Dittmer, J. J.; Alivisatos, A. P. Hybrid Nanorod-Polymer Solar Cells. *Science* **2002**, *295*, 2425–2427.
10. McDonald, S. A.; Konstantatos, G.; Zhang, S.; Cyr, P. W.; Klem, E. J. D.; Levina, L.; Sargent, E. H. Solution-Processed PbS Quantum Dot Infrared Photodetectors and Photovoltaics. *Nat. Mater.* **2005**, *4*, 138–142.
11. Ellingson, R. J.; Beard, C. M.; Johnson, J. C.; Yu, P.; Micic, O. I.; Nozik, A. J.; Shabaev, A.; Efros, A. L. Highly Efficient Multiple Exciton Generation in Colloidal PbSe and PbS Quantum Dots. *Nano Lett.* **2005**, *5*, 865–871.
12. Leschkies, K. S.; Divakar, R.; Basu, J.; Enache-Pommer, E.; Boercker, J. E.; Carter, C. B.; Kortshagen, U. R.; Norris, D. J.; Aydil, E. S. Photosensitization of ZnO Nanowires with CdSe Quantum Dots for Photovoltaic Devices. *Nano Lett.* **2007**, *7*, 1793.
13. Maria, A.; Cyr, P. W.; Klern, E. J. D.; Levina, L.; Sargent, E. H. Solution-Processed Infrared Photovoltaic Devices with >10% Monochromatic Internal Quantum Efficiency. *Appl. Phys. Lett.* **2005**, *87*, 213112.
14. Kim, S. J.; Kim, W. J.; Cartwright, A. N.; Prasad, P. N. Carrier Multiplication in a PbSe Nanocrystal and P3HT/PCBM Tandem Cell. *Appl. Phys. Lett.* **2008**, *92*, 191107.
15. Gur, I.; Fromer, N. A.; Geier, M. L.; Alivisatos, A. P. Air-Stable All-Inorganic Nanocrystal Solar Cells Processed From Solution. *Science* **2005**, *310*, 462–465.
16. Guo, Q.; Kim, S. J.; Kar, M.; Shafarman, W. N.; Birkmire, R. W.; Stach, E. A.; Agrawal, R.; Hillhouse, H. W. Development of $CuInSe_2$ Nanocrystal and Nanoring Inks for Low-Cost Solar Cells. *Nano Lett.* **2008**, *8*, 2982–2987.
17. Leschkies, K. S.; Beatty, T. J.; Kang, M. S.; Norris, D. J.; Aydil, E. S. Solar Cells Based on Junctions between Colloidal PbSe Nanocrystals and Thin ZnO Films. *ACS Nano* **2009**, *3*, 3638–3648.
18. Ma, W.; Luther, J. M.; Zheng, H. M.; Wu, Y.; Alivisatos, A. P. Photovoltaic Devices Employing Ternary PbS_xSe_{1-x} Nanocrystals. *Nano Lett.* **2009**, *9*, 1699–1703.
19. Riha, S. C.; Fredrick, S. J.; Sambur, J. B.; Liu, Y.; Prieto, A. L.; Parkinson, B. A. Photoelectrochemical Characterization of Nanocrystalline Thin-Film Cu_2ZnSnS_4 Photocathodes. *ACS Appl. Mater. Interfaces* **2011**, *3*, 58–66.

20. Mora-Sero, I.; Bisquert, J.; Dittrich, T.; Belaidi, A.; Susha, A. S.; Rogach, A. L. Photosensitization of TiO_2 Layers with CdSe Quantum Dots: Correlation between Light Absorption and Photoinjection. *J. Phys. Chem. C* **2007**, *111*, 14889–14892.
21. Yu, P. R.; Zhu, K.; Norman, A. G.; Ferrere, S.; Frank, A. J.; Nozik, A. J. Nanocrystalline TiO_2 Solar Cells Sensitized with InAs Quantum Dots. *J. Phys. Chem. B* **2006**, *110*, 25451.
22. Luther, J. M.; Law, M.; Song, Q.; Reese, M. O.; Beard, M. C.; Ellingson, R. J.; Nozik, A. J. Schottky Solar Cells Based on Colloidal Nanocrystal Films. *Nano Lett.* **2008**, *8*, 3488–3492.
23. Debnath, R.; Tang, J.; Barkhouse, D. A.; Wang, X.; Pattantyus-Abraham, A. G.; Brzozowski, L.; Levina, L.; Sargent, E. H. Ambient-Processed Colloidal Quantum Dot Solar Cells *via* Individual Pre-encapsulation of Nanoparticles. *J. Am. Chem. Soc.* **2010**, *132*, 5952–5953.
24. Ma, W.; Swisher, S. L.; Ewers, T.; Engel, J.; Ferry, V. E.; Atwater, H. A.; Alivisatos, A. P. Photovoltaic Performance of Ultrasmall PbSe Quantum Dots. *ACS Nano* **2011**, *5*, 8140–8147.
25. Acharya, K. P.; Khon, E.; O'Connor, T.; Nemitz, I.; Klinkova, A.; Khnayzer, R. S.; Anzenbacher, P.; Zamkov, M. Heteroepitaxial Growth of Colloidal Nanocrystals onto Substrate Films *via* Hot-Injection Routes. *ACS Nano* **2011**, *5*, 4953–4964.
26. Wang, Q.; Zhu, K.; Neale, N. R.; Frank, A. J. Constructing Ordered Sensitized Heterojunctions: Bottom-Up Electrochemical Synthesis of p-Type Semiconductors in Oriented n-TiO_2 Nanotube Arrays. *Nano Lett.* **2009**, *9*, 806–813.
27. Ip, A. H.; Thon, S. M.; Hoogland, S.; Voznyy, O.; Zhitomirsky, D.; Debnath, R.; Levina, L.; Rollny, L. R.; Carey, G. H.; Fischer, A.; *et al.* Hybrid Passivated Colloidal Quantum Dot Solids. *Nat. Nanotechnol.* **2012**, *7*, 577–582.
28. Coe, S.; Woo, W. K.; Bawendi, M.; Bulovic, V. Electroluminescence from Single Monolayers of Nanocrystals in Molecular Organic Devices. *Nature* **2002**, *420*, 800–803.
29. Tessler, N.; Medvedev, V.; Kazes, M.; Kan, S. H.; Banin, U. Efficient Near-Infrared Polymer Nanocrystal Light-Emitting Diodes. *Science* **2002**, *295*, 1506–1508.
30. Steckel, J. S.; Snee, P. T.; Coe-Sullivan, S.; Zimmer, J. P.; Halpert, J. E.; Anikeeva, P. O.; Kim, L. A.; Bulovic, V.; Bawendi, M. G. Color-Saturated Green-Emitting QD-LEDs. *Angew. Chem., Int. Ed.* **2006**, *45*, 5796–5799.
31. Colvin, V. L.; Schlamp, M. C.; Alivisatos, A. P. Light-Emitting-Diodes Made from Cadmium Selenide Nanocrystals and a Semiconducting Polymer. *Nature* **1994**, *370*, 354–357.
32. Schlamp, M. C.; Peng, X. G.; Alivisatos, A. P. Improved Efficiencies in Light Emitting Diodes Made with CdSe(CdS) Core/Shell Type Nanocrystals and a Semiconducting Polymer. *J. Appl. Phys.* **1997**, *82*, 5837–5842.
33. Mattoussi, H.; Radzilowski, L. H.; Dabbousi, B. O.; Thomas, E. L.; Bawendi, M. G.; Rubner, M. F. Electroluminescence from Heterostructures of Poly(phenylene vinylene) and Inorganic CdSe Nanocrystals. *J. Appl. Phys.* **1998**, *83*, 7965–7974.
34. Sun, Q.; Wang, A. Y.; Li, L. S.; Wang, D.; Zhu, T.; Xu, J.; Yang, C.; Li, Y. Bright, Multicoloured Light-Emitting Diodes Based on Quantum Dots. *Nat. Photonics* **2007**, *1*, 717–722.
35. Beaulac, R.; Archer, P. I.; Ochsenbein, S. T.; Gamelin, D. R. Mn^{2+}-Doped CdSe Quantum Dots: New Inorganic Materials for Spin-Electronics and Spin-Photonics. *Adv. Funct. Mater.* **2008**, *18*, 3873–3891.
36. Caruge, J. M.; Halpert, J. E.; Wood, V.; Bulovic, V.; Bawendi, M. G. Colloidal Quantum-Dot Light-Emitting Diodes with Metal-Oxide Charge Transport Layers. *Nat. Photonics* **2008**, *2*, 247–250.
37. Wang, R. Y.; Feser, J. P.; Lee, J. S.; Talapin, D. V.; Segalman, R.; Majumdar, A. Enhanced Thermopower in PbSe Nanocrystal Quantum Dot Superlattices. *Nano Lett.* **2008**, *8*, 2283–2288.
38. Kovalenko, M. V.; Scheele, M.; Talapin, D. V. Colloidal Nanocrystals with Molecular Metal Chalcogenide Surface Ligands. *Science* **2009**, *324*, 1417–1420.
39. Ridley, B. A.; Nivi, B.; Jacobson, J. M. All-Inorganic Field Effect Transistors Fabricated by Printing. *Science* **1999**, *286*, 746–749.
40. Lee, S.; Jeong, S.; Kim, D.; Park, B. K.; Moon, J. Fabrication of a Solution-Processed Thin-Film Transistor Using Zinc Oxide Nanoparticles and Zinc Acetate. *Superlattices Microstruct.* **2007**, *42*, 361–368.
41. Schneider, J. J.; Hoffmann, R. C.; Engstler, J.; Soffke, O.; Jaegermann, W.; Issanin, A.; Klyszcz, A. A. A Printed and Flexible Field-Effect Transistor Device with Nanoscale Zinc Oxide as Active Semiconductor Material. *Adv. Mater.* **2008**, *20*, 3383–3387.
42. Talapin, D. V.; Mekis, L.; Gotzinger, S.; Kornowski, A.; Benson, O.; Weller, H. CdSe/CdS/ZnS and CdSe/ZnSe/ZnS Core–Shell–Shell Nanocrystals. *J. Phys. Chem. B* **2004**, *108*, 18826–18831.
43. Talapin, D. V.; Murray, C. B. PbSe Nanocrystal Solids for n- and p-Channel Thin Film Field-Effect Transistors. *Science* **2005**, *310*, 86–89.
44. Lee, J. S.; Shevchenko, E. V.; Talapin, D. V. Au-PbS Core–Shell Nanocrystals: Plasmonic Absorption Enhancement and Electrical Doping *via* Interparticle Charge Transfer. *J. Am. Chem. Soc.* **2008**, *130*, 9673–9675.
45. Lee, J. S.; Kovalenko, M. V.; Huang, J.; Chung, D. S.; Talapin, D. V. Band-like Transport, High Electron Mobility and High Photoconductivity in All-Inorganic Nanocrystal Arrays. *Nat. Nanotechnol.* **2011**, *6*, 348–352.
46. Guyot-Sionnest, P. Electrical Transport in Colloidal Quantum Dot Films. *J. Phys. Chem. Lett.* **2012**, *3*, 1169–1175.
47. Tang, J.; Sargent, E. H. Infrared Colloidal Quantum Dots for Photovoltaics: Fundamentals and Recent Progress. *Adv. Mater.* **2011**, *23*, 12–29.
48. Talapin, D. V.; Lee, J. S.; Kovalenko, M. V.; Shevchenko, E. V. Prospects of Colloidal Nanocrystals for Electronic and Optoelectronic Applications. *Chem. Rev.* **2010**, *110*, 389–458.
49. Gai, I.; Peng, H.; Li, J. Electronic Properties of Nonstoichiometric PbSe Quantum Dots from First Principles. *J. Phys. Chem. C* **2009**, *113*, 21506–21511.
50. Tang, J.; Kemp, K. W.; Hoogland, S.; Jeong, K. S.; Liu, H.; Levina, L.; Furukawa, M.; Wang, X.; Debnath, R.; Cha, D.; *et al.* Colloidal-Quantum-Dot Photovoltaics Using Atomic-Ligand Passivation. *Nat. Mater.* **2011**, *10*, 765–771.
51. Liu, Y.; Gibbs, M.; Perkins, C. L.; Tolentino, J.; Zarghami, M. H.; Bustamante, J.; Law, M. Robust, Functional Nanocrystal Solids by Infilling with Atomic Layer Deposition. *Nano Lett.* **2011**, *11*, 5349–5355.
52. Mashford, B.; Baldauf, J.; Nguyen, T. L.; Funston, A. M.; Mulvaney, P. Synthesis of Quantum Dot Doped Chalcogenide Glasses *via* Sol–Gel Processing. *J. Appl. Phys.* **2011**, *109*, 094305.
53. Kinder, E.; Moroz, P.; Diederich, G.; Johnson, A.; Kirsanova, M.; Nemchinov, A.; O'Connor, T.; Roth, D.; Zamkov, M. Fabrication of All-Inorganic Nanocrystal Solids through Matrix Encapsulation of Nanocrystal Arrays. *J. Am. Chem. Soc.* **2011**, *133*, 20488–20499.
54. Khon, E.; Lambright, S.; Khon, D.; Smith, B.; O'Connor, T.; Moroz, P.; Imboden, M.; Diederich, G.; Perez-Bolivar, D.; Anzenbacher, P.; *et al.* Inorganic Solids of CdSe Nanocrystals Exhibiting High Emission Quantum Yield. *Adv. Funct. Mater.* **2012**, *22*, 3714–3722.
55. Choi, J.-H.; Fafarman, A. T.; Oh, S. J.; Ko, D.-K.; Kim, D. K.; Diroll, B. T.; Muramoto, S.; Gillen, J. G.; Murray, C. B.; Kagan, C. R. Bandlike Transport in Strongly Coupled and Doped Quantum Dot Solids: A Route to High-Performance Thin-Film Electronics. *Nano Lett.* **2012**, *12*, 2631–2638.
56. Mott, N. F. Electrons in Disordered Structures. *Adv. Phys.* **1967**, *16*, 49.
57. Bose, R.; McMillan, J. F.; Gao, J.; Rickey, K. M.; Chen, C. J.; Talapin, D. V.; Murray, C. B.; Wong, C. W. Temperature-Tuning of Near-Infrared Monodisperse Quantum Dot Solids at 1.5 μm for Controllable Forster Energy Transfer. *Nano Lett.* **2008**, *8*, 2006–2011.
58. Pietryga, J. M.; Werder, D. J.; Williams, D. J.; Casson, J. L.; Schaller, R. D.; Klimov, V. I.; Hollingsworth, J. A. Utilizing the Lability of Lead Selenide To Produce Heterostructured Nanocrystals with Bright, Stable Infrared Emission. *J. Am. Chem. Soc.* **2008**, *130*, 4879–4885.

59. Pathan, H. M.; Lokhande, C. D. Deposition of Metal Chalcogenide Thin Films by Successive Ionic Layer Adsorption and Reaction (SILAR) Method. *Bull. Mater. Sci.* **2004**, *27*, 85–111.
60. Chandler, R. E.; Houtepen, A. J.; Nelson, J.; Vanmaekelbergh, D. Electron Transport in Quantum Dot Solids: Monte Carlo Simulations of the Effects of Shell Filling, Coulomb Repulsions, and Site Disorder. *Phys. Rev. B* **2007**, *75*, 085325-10.
61. Pattantyus-Abraham, A. G.; Kramer, I. J.; Barkhouse, A. R.; Wang, X.; Konstantatos, G.; Debnath, R.; Levina, L.; Raabe, I.; Nazeeruddin, M. K.; Gratzel, M.; *et al.* Depleted-Heterojunction Colloidal Quantum Dot Solar Cells. *ACS Nano* **2010**, *4*, 3374–3380.
62. Zhitomirsky, D.; Voznyy, O.; Hoogland, S.; Sargent, E. H. Measuring Charge Carrier Diffusion in Coupled Colloidal Quantum Dot Solids. *ACS Nano* **2013**, *7*, 5282–5290.
63. Hines, M. A.; Scholes, G. D. Colloidal PbS Nanocrystals with Size-Tunable Near-Infrared Emission: Observation of Post-Synthesis Self-Narrowing of the Particle Size Distribution. *Adv. Mater.* **2003**, *15*, 1844–1849.